Enhanced Incident Photon-to-Electron Conversion Efficiency of Tungsten Trioxide Photoanodes Based on 3D-Photonic Crystal Design

Xiaoqing Chen,[†,‡,§] Jinhua Ye,[†,‡,*] Shuxin Ouyang,[‡] Tetsuya Kako,[†,‡] Zhaosheng Li,[§] and Zhigang Zou[§]

[†]Department of Chemistry, Graduate School of Science, Hokkaido University, Sapporo 060-0810, Japan, [‡]Photocatalytic Materials Center, National Institute for Materials Science, 1-2-1 Sengen, Tsukuba, Ibaraki 305-0047, Japan, and [§]Ecomaterials and Renewable Energy Research Center, Department of Physics, Nanjing University, Nanjing 210093, China

ABSTRACT In this study, 3D-photonic crystal design was utilized to enhance incident photon-to-electron conversion efficiency (IPCE) of WO_3 photoanodes. Large-area and high-quality WO_3 photonic crystal photoanodes with inverse opal structure were prepared. The photonic stop-bands of these WO_3 photoanodes were tuned experimentally by variation of the pore size of inverse opal structures. It was found that when the red-edge of the photonic stop-band of WO_3 inverse opals overlapped with the WO_3 electronic absorption edge at E_g = 2.6−2.8 eV, a maximum of 100% increase in photocurrent intensity was observed under visible light irradiation ($\lambda > 400$ nm) in comparison with a disordered porous WO_3 photoanode. When the red-edge of the stop-band was tuned well within the electronic absorption range of WO_3, noticeable but less amplitude of enhancement in the photocurrent intensity was observed. It was further shown that the spectral region with a selective IPCE enhancement of the WO_3 inverse opals exhibited a blue-shift in wavelength under off-normal incidence of light, in agreement with the calculated stop-band edge locations. The enhancement could be attributed to a longer photon−matter interaction length as a result of the slow-light effect at the photonic stop-band edge, thus leading to a remarkable improvement in the light-harvesting efficiency. The present method can provide a potential and promising approach to effectively utilize solar energy in visible-light-responsive photoanodes.

KEYWORDS: photon-to-electron conversion · WO_3 photoanode · inverse opal · stop-band · slow light

Hydrogen is a promising candidate as a future energy carrier. The conversion of solar energy into hydrogen represents an attractive but challenging alternative for photoelectrochemical cells, following the pioneer work on TiO_2 photoanodes for hydrogen production by Fujishima and Honda.[1] Unfortunately, owing to its wide electronic band gap (3.0−3.2 eV), TiO_2 absorbs only the ultraviolet fraction of the solar spectrum, which accounts for just 4% of solar irradiation.[2−4] This unavoidably leads to low utilization efficiency for solar light.[2] Consequently, a few oxide semiconductors with narrower band gaps, for example, tungsten trioxide (band gap, E_g = 2.6−2.8 eV), have attracted more and more attention as photoanode materials because of their visible light response and good photochemical stability.[5−11] Porous structures are used to improve the incident photon-to-electron conversion efficiency (IPCE) of WO_3 photoanodes. For example, Santato *et al*. have reported that the nanocrystalline WO_3 photoanodes with porous structures exhibited a high IPCE from acidic solution.[5−7] Berger *et al*. have demonstrated that random porous layers of WO_3 produced significantly higher photocurrent efficiency than a compact layer.[8] These results suggest the advantage of constructing the porous network of WO_3, *i.e*., high specific surface area to increase the density of active sites at which the redox reactions can take place.[12] For further refinement of the porous WO_3 photoanode, improving its solar light harvesting to enhance IPCE is a critical challenge because the light absorption around the electronic absorption edge of WO_3 is still limited.[6]

Photonic-crystal-based optical coupling[13] offers a unique way of light−matter interaction to increase light harvesting, especially around the absorption edge of a semiconductor. A photonic crystal is a periodic dielectric structure that can forbid the propagation of light in a certain crystal direction within a certain spectrum regime, called a photonic stop-band.[14] The light in a photonic crystal undergoes strong coherent multiple scattering and travels with very low group velocity near the photonic stop-band edges, referred to as slow light.[15,16] Such a slow-light effect can considerably increase the effective optical path length, therefore leading to a delay and storage of light in photonic materials.[16]

* Address correspondence to Jinhua.Ye@nims.go.jp.

Received for review August 27, 2010 and accepted May 23, 2011.

Published online May 23, 2011
10.1021/nn200100v

Order-of-magnitude absorption enhancement was reported in a tungsten woodpile structure at the photonic band edge by Lin *et al.*[17] This enhancement was understood as a result of the slow-light effect, a longer photon−matter interaction length, and a finite intrinsic absorption of tungsten material.[17] Absorption and thermal emission enhancement, which was also caused by the slow optical group velocity that occurred near the edge of the metallicity gap, have been observed in molybdenum and tungsten woodpile structures by Nagpal *et al.*[18] In addition to metallic photonic crystals, the slow-light effect could be exploited to enhance the interaction of light with photoresponsive semiconductors and amplify photochemical reactions. The slow-light effect on photovoltaic cells and the photochemical process was investigated by Nishimura *et al.*[19] and Chen *et al.*[20−22] as a means of promoting the optical absorbance of TiO_2-based composite system. Since then, this effect has been utilized for the enhancement in efficiencies of dye-sensitized TiO_2 solar cells and TiO_2-based photocatalytic reactions.[23−29] The slow-light effect in a photonic crystal thus provides a strategy for modifying the intrinsic optical interactions inside a material. Considering the superiorities of nanocrystalline WO_3 as a photoanode material, if slow-light propagation modes in the inverse opal WO_3 structure is designed to be resonant with a specific light frequency around its electronic absorption edge, the interaction of WO_3 with that frequency of light should be greatly increased, which may improve obviously its IPCE. To our knowledge, there is yet no study available on the WO_3 inverse opal photoanode focusing on a correlation between the slow-light effect and IPCE. It is noted that fabrication of a well-ordered and crack-free macroporous structure in a large area is critical to observe an obvious effect induced by photonic stop-bands of WO_3 inverse opals.

In this article, WO_3 inverse opals with high optical quality were synthesized using the forced impregnation approach presented in our previous work.[30] In order to study the slow-light effect on the photoelectrochemical properties of WO_3, WO_3 inverse opals with different stop-bands were produced by the template spheres with different sizes, which dictated the pore sizes in the inverse opal structures. With this approach, the stop-bands in WO_3 inverse opals could be tuned either into or out of the electronic absorption band gap of WO_3. For comparison, we also prepared disordered porous and unpatterned nonporous WO_3 photoanodes, which did not exhibit any slow-light effect. We demonstrated that the slow-light effect in WO_3 inverse opals could lead to a remarkable enhancement in the photoelectric conversion, compared with the disordered porous and unpatterned WO_3 photoanodes. We also found that the WO_3 inverse opals showed selective light harvesting and IPCE enhancement in the spectral region corresponding to their respective slow-light locations at both normal and off-normal incidence of light.

RESULTS AND DISCUSSION

The stop-bands of WO_3 inverse opals are tunable by varying the pore sizes, according to the modified Bragg's law as the following equation:[31]

$$\lambda = 2\sqrt{\frac{2}{3}}D\sqrt{n_{WO_3}^2 f + n_{void}^2(1-f) - \sin^2\theta} \quad (1)$$

where λ is the wavelength derived from the stop-band, D is the pore size of the inverse opal, n_{WO3} and n_{void} are the refractive index of WO_3 and the voids respectively, f is the WO_3 phase volume percentage, which is generally taken as 0.26, and θ is the incident angle of light. For normal incidence, $\theta = 0°$. According to eq 1 and considering the shrinkage ($\sim$ 30%) of the pore size of the inverse opal during the removal of the polystyrene (PS) template by sintering,[30] three kinds of template spheres (diameter: 200, 260, and 360 nm) were selected to fabricate WO_3 inverse opals with their stop-bands estimated to be into, overlapped with, and out of the electronic absorption edge of WO_3, respectively.

The opal templates composed of the PS spheres with the diameters of 200, 260, and 360 nm were prepared following the convective self-assembly method.[32] Figure 1a−c shows that the PS spheres are hexagonally close-packed in a large area. This high degree of ordering is confirmed by the uniform and brilliant colors reflected from the sample surface, which are caused by Bragg diffraction of visible light, as observed in Figure 1d. The measured transmission spectra for the three opal templates are shown in Figure 1e. In each case, a pronounced attenuation dip (correspondingly 457, 583, and 819 nm) is clearly observed, which also indicates the well long-range ordering of these samples. These sharp transmission dips are attributed to the stop-bands that open along the Γ−L direction in the reciprocal space of these highly ordered opal templates.[33,34]

The WO_3 photoanodes with inverse opal structure were fabricated using the colloidal crystal templates. In order to penetrate the precursor of WO_3 into the interstices in the templates completely, the forced impregnation approach[30] was used for precursor infiltration. The fabrication details are given in the experimental section. The WO_3 inverse opals fabricated from 200, 260, and 360 nm of PS-sphere arrays are denoted as WO_3-200, WO_3-260, and WO_3-360, respectively. Black holes connecting the neighboring pores are observed in the SEM images of the as-prepared WO_3 inverse opals (Figure 2a−c), indicating that the spherical pores in the WO_3 photonic crystals are three-dimensionally ordered in a hexagonal close-packed array. The average pore sizes in Figure 2a−c are about 140 ± 10, 170 ± 10, and 230 ± 10 nm, respectively,

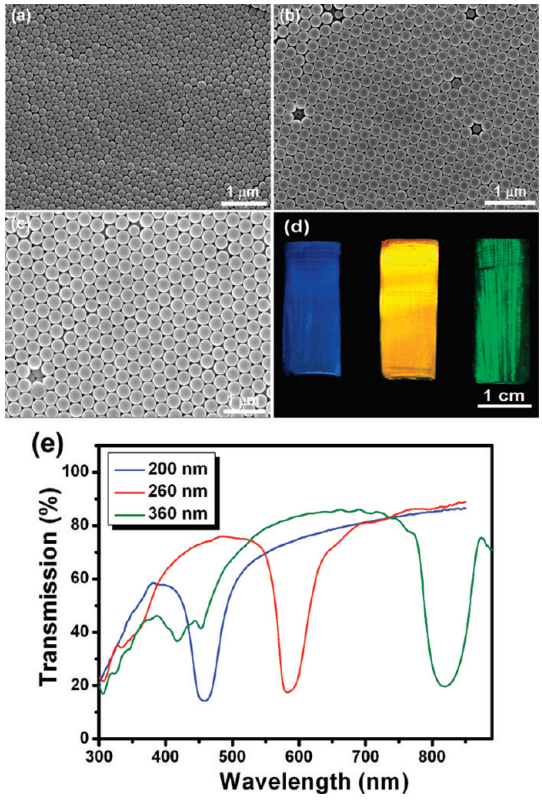

Figure 1. SEM images of colloidal crystal templates self-assembled from PS spheres with different diameters: (a) 200 nm, (b) 260 nm, and (c) 360 nm. (d) Photograph of the PS opals under white light illumination; sphere diameter is 200, 260, and 360 nm, respectively, from left to right. (e) Transmission spectra of the PS opals measured at a normal incidence of light.

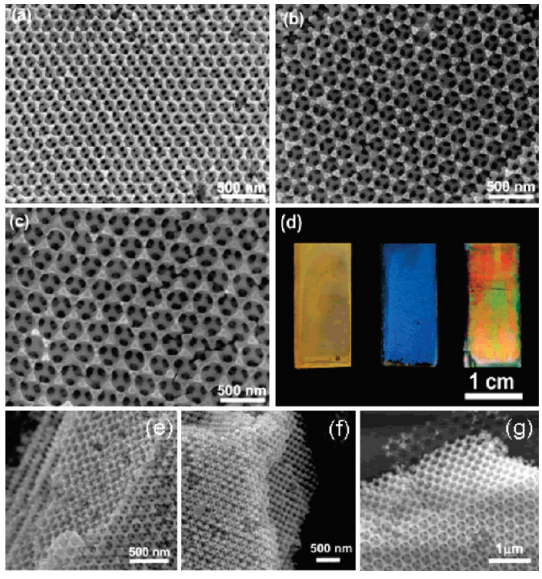

Figure 2. SEM images of WO_3 inverse opals: (a) WO_3-200, (b) WO_3-260, and (c) WO_3-360. (d) Photograph of the inverse opal WO_3 photoanodes under white light illumination, WO_3-200, WO_3-260, and WO_3-360, from left to right. (e–g) SEM images of cross-section view of each inverse opal. The thickness is estimated to be about 2.5 μm (17 layers) for WO_3-200 (e), 2.6 μm (14 layers) for WO_3-260 (f), and 2.7 μm (11 layers) for WO_3-360 (g).

which show 25–35% shrinkage in comparison with the primary PS spheres. In Figure 2d, the WO_3-200, WO_3-260, and WO_3-360 inverse opals show yellow, blue, or red-green in reflection mode under illumination of white light, respectively, as a result of the stop-band centered at different wavelengths. Figure 2d shows that the color of each inverse opal sample is quite uniform after precursor infiltration and annealing processes, illustrating an excellent periodicity over a range of centimeter length scale. As shown in Figure 2e–g, the cross-section SEM images of all the inverse opals also exhibit vertical ordering. The thickness of all the prepared WO_3 photoanodes with face-centered-cubic (fcc) packing structure is measured as around 2.6 μm, indicating that their effective light absorption thickness is comparable. In addition, as one of the reference samples, a disordered porous WO_3 structure (see inset SEM image in Figure 3b) was also fabricated with the same thickness under the same conditions as the inverse opals. But it was prepared from a randomly packed template formed with a mixture of 200, 260, and 360 nm PS spheres. The unpatterned WO_3 photoanode with a thickness of approximately 2.5 μm (see inset SEM image in Figure 3c) was fabricated by spin coating using the same precursor. As shown in Figure 3, the XRD patterns of all the samples match the Joint Committee on Powder Diffraction Standards File (JCPDS No. 01-075-2072), which confirms the monoclinic phase of these WO_3 microstructures.

The existence of stop-bands of these WO_3 inverse opal photoanodes was confirmed in the measurement of light reflection spectra. Figure 4 illustrates the measured light reflection spectra of three WO_3 inverse opals with different stop-bands as well as the disordered porous and the unpatterned samples. It is known that the WO_3 electronic band gap is around 2.6 eV, corresponding to a wavelength of around 470 nm.[2] This explains why the reflection spectra for all the WO_3 photoanodes begin to attenuate sharply as the wavelength becomes shorter than 470 nm, which is caused by strong intrinsic absorption of light in the WO_3 semiconductor. The formation of high-quality inverse opal structure can result in a Bragg reflection peak at wavelengths relative to the photonic stop-band center.[35,36] For the spectrum of the WO_3-260 inverse opal, a Bragg reflection peak centered at 415 nm is observed. A reflection peak at 345 nm located in the electronic absorption range of WO_3 is observed for the WO_3-200 inverse opal. For the WO_3-360 inverse opal, a broad reflection peak at 580 nm is observed, which is also due to the stop-band reflection effect. The notch at the long-wavelength side of the reflection peak (marked by the colored circle) in the reflection spectrum of each inverse opal structure indicates their respective position of the slow light.

To confirm that slow light has an enhancement effect on the light harvesting, the absorption spectra

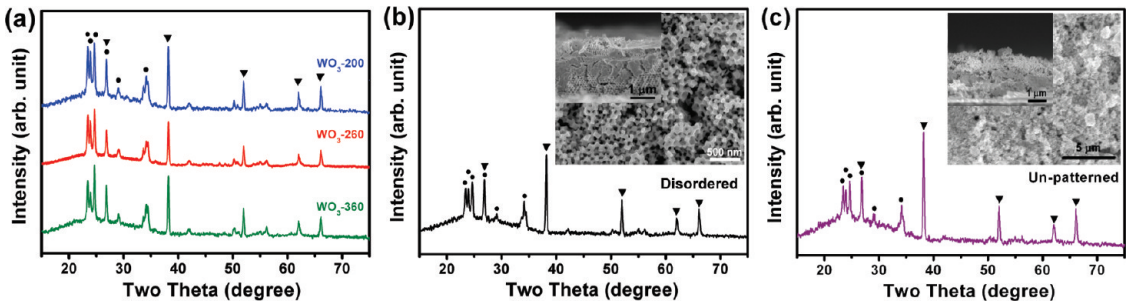

Figure 3. XRD patterns of three inverse opals WO_3 photoanodes (a), a disordered porous WO_3 (b), and an unpatterned WO_3 (c) calcined at 475 °C for 2 h indicate the monoclinic phase of WO_3 in each sample. Monoclinic phase of WO_3 (●); FTO substrate (▼). The insets in (b) and (c) show the SEM images of the disordered porous WO_3 and the unpatterned WO_3 samples (top view and cross-section view).

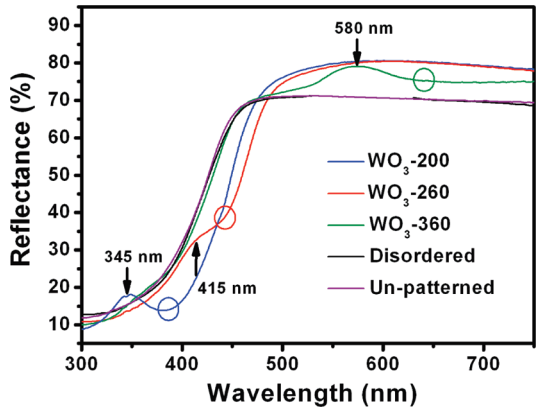

Figure 4. Light reflectance spectra of the WO_3 inverse opals, a disordered porous WO_3, and an unpatterned WO_3 photoanode, measured at a normal incidence of light. Centers of the stop-bands are marked by black arrows. The locations of slow light at the red-edge of stop-band for each inverse opal are shown as colored hollow circles.

of WO_3 inverse opal photoanodes as well as the disordered porous and the unpatterned samples are shown in Figure 5a. It is apparent that there is absorption enhancement in the specific region corresponding to the location of the slow light at the red-edge of the stop-band in each inverse opal sample, as indicated by the colored circles. For example, the enhanced absorption of the WO_3-360 photoanode is in the vicinity of 630 nm, which is out of the electronic absorption range of WO_3. To reveal that there is a specific spectral region in which the absorption is enhanced for each WO_3 inverse opal, the absorption spectra of the inverse opal samples are normalized to that of the unpatterned sample. The resultant absorbance enhancement spectra are shown in Figure 5b. It is obvious that the WO_3-200 and WO_3-260 inverse opals show an enhanced absorption in a certain specific region that depends on the location of their respective stop-band edge. These regions show a good match with the wavelengths of the slow light for each inverse opal sample. For the WO_3-200 photoanode, the absorption enhancement relative to the unpatterned sample is located in the electronic absorption of WO_3 in the region of 350–420 nm. This spectral region corresponds to the red-edge of its stop-band of the WO_3-200 photoanode. For the WO_3-260 photoanode the enhanced absorption is in the region of 420–460 nm, which is at the electronic absorption edge of WO_3 and also at its stop-band red-edge.

To investigate the characteristics of these WO_3 inverse opals as photoanodes, photoelectrochemical analysis was performed on them as well as the disordered porous WO_3 and the unpatterned WO_3 photoanodes. Figure 6a shows photocurrent–potential curves measured under UV–visible light irradiation ($\lambda > 300$ nm). Porous samples including the inverse opals and disordered porous WO_3 photoanodes exhibit higher photocurrent intensities than the unpatterned nonporous WO_3 photoanode, because multiple scattering in the porous structure can improve light harvesting and the electrolyte can easily be infiltrated through the pores, inducing more effective redox reactions at the WO_3–electrolyte interface.[8,35] All the WO_3 inverse opals have higher photocurrent intensities than the disordered porous WO_3 sample, which may be attributed to the following reasons. First, compared with the disordered porous WO_3, which has numerous collapsed structures and discontinuous pore walls (see inset in Figure 3b), the spherical macropores are periodically arranged with excellent connectivity in the inverse opals. This interconnected framework can facilitate efficient charge transport to a conducting substrate.[35] Another benefit is the enhanced light–matter interaction due to the slow-light effect, which will be discussed later. It is noted that under the irradiation of UV–visible light ($\lambda > 300$ nm), the photocurrent intensity of the WO_3-260 sample is 200% that of the disordered porous WO_3 photoanode and 250% that of the unpatterned one, respectively, and also higher than those of WO_3-200 and WO_3-360 inverse opals. As WO_3 is visible-light sensitive, we further evaluated the photoelectrochemical properties of all the photoanodes under visible light irradiation ($\lambda > 400$ nm), which is presented in Figure 6b. The observed results are similar to those under UV–visible light irradiation ($\lambda > 300$ nm). In this case, the WO_3-260 photoanode produces 2-fold photocurrent intensity as

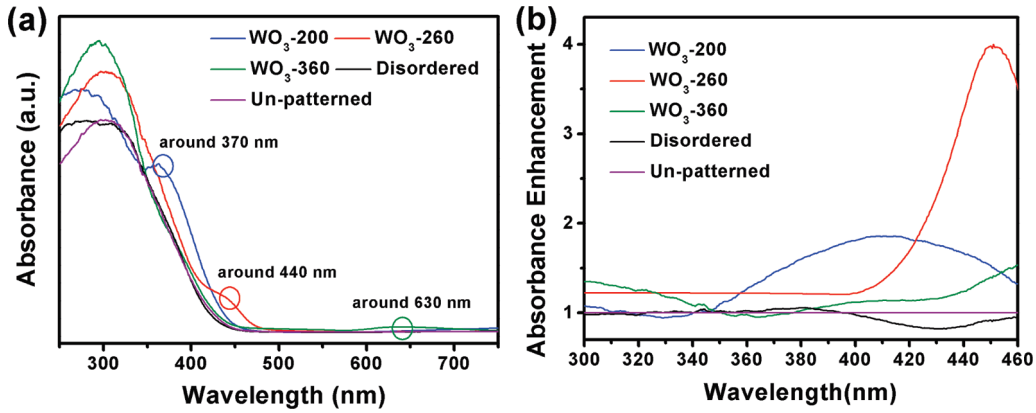

Figure 5. (a) Light absorption spectra of WO_3 inverse opals, a disordered porous WO_3, and an unpatterned WO_3 photoanode, measured at a normal incidence of light. The colored hollow circles show the slow-light absorption at the red-edge of the stop-band for each inverse opal structure. (b) Absorbance enhancement spectra (ratio of the absorbance of WO_3 inverse opals and disordered porous sample to that of the unpatterned WO_3 photoanode) as a function of the wavelength.

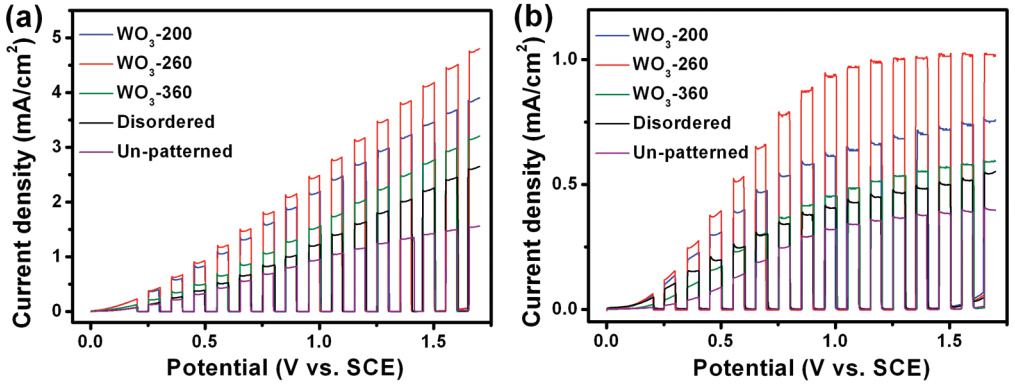

Figure 6. (a) Photocurrent−potential curves of all the prepared WO_3 photoanodes measured under UV−visible light irradiation (λ > 300 nm). (b) Photocurrent−potential curves measured under visible light irradiation (λ > 400 nm).

compared with the disordered porous sample. The WO_3-200 and WO_3-360 inverse opals show about 30% and 43% decrease in photocurrent intensity in comparison with the WO_3-260 photoanode, respectively.

Among all the WO_3 inverse opal photoanodes, the photocurrent intensity of the WO_3-260 sample for both UV−visible light and visible light irradiation is mostly enhanced. Due to our elaborate choice of the template sphere size according to eq 1, the resultant slow-light wavelength for the WO_3-260 inverse opal is thus overlapped with the electronic absorption edge of WO_3. As presented in its reflection and absorption spectra (Figure 4 and Figure 5a), its slow light is in the vicinity of 440 nm. In this case, the slow light of WO_3-260 is trapped in the WO_3 matrix by multiple scattering and diffraction, which induces much stronger interaction of light with the dielectric matrix,[19,20] thus generating much more photoinduced carriers in WO_3. It is indicated that this overlapping of slow light with the electronic absorption edge of WO_3 will result in an increased light absorption (as shown in Figure 5a) as well as the enhanced light utilization for photoelectric conversion.

In contrast, the photocurrent intensity for the WO_3-200 is lower than that of the WO_3-260 sample, but still higher than that of WO_3-360. The slow light for WO_3-200 is in the vicinity of 370 nm and well within the strong electronic absorption region of WO_3 (Figure 5a). As a consequence, a contribution to light harvesting due to the slow-light effect is expected. The increase of light absorption induced by the slow-light effect in the WO_3-200 inverse opal is extended to the onset of the visible region, as shown by Figure 5a. Therefore, its photocurrent intensity is still higher than those of the WO_3-360 as well as the disordered porous and the unpatterned WO_3 photoanodes under visible light irradiation (λ > 400 nm). However, since the intrinsic absorption around the electronic absorption edge of WO_3 (420−470 nm) is much more limited than that around 300−400 nm (see the intrinsic absorption spectrum of monoclinic WO_3, *i.e.*, the absorption spectrum of the unpatterned sample in Figure 5a), the photocurrent enhancement of the WO_3-260 inverse opal owing to the slow-light effect is more intense than that of the WO_3-200 sample. For the WO_3-360 inverse opal, the stop-band moves out of the electronic absorption of WO_3 due to its larger spherical pores.

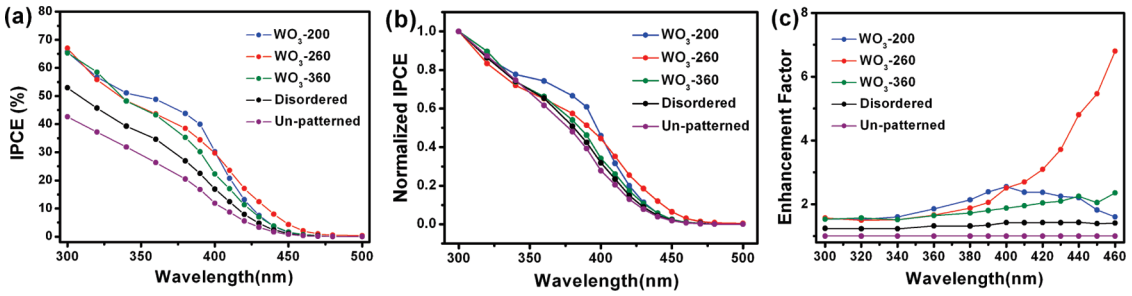

Figure 7. (a) IPCE plots of all the microstructured WO_3 photoanodes. All the reactions were carried out with 0.8 V of applied bias. (b) Relative spectral IPCE of all the microstructured WO_3 photoanodes normalized at a wavelength of 300 nm. (c) IPCE enhancement factor (the ratio of the IPCE of WO_3 inverse opals and disordered porous sample to that of the unpatterned WO_3 photoanode) as a function of the wavelength.

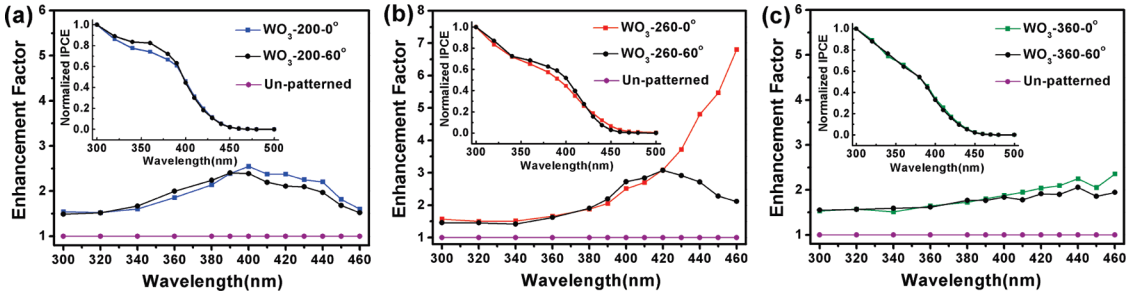

Figure 8. IPCE enhancement factor spectra of the WO_3 inverse opals with light irradiation at $\theta = 0°$ and 60° (ratio of the IPCE of WO_3 inverse opals at two different incident angles to that of unpatterned sample at 0° incidence). The inset in each figure shows the normalized IPCE curves at 0° and 60° incidence.

Although in this case the slow light near the red-edge of the stop-band will not lead to a remarkable photocurrent enhancement, other mechanisms of light propagation in photonic crystals can affect the photon-conversion efficiency of the WO_3-360 photoanode, including Bragg diffraction by the periodic lattice[37] and multidirectional internal scattering from defects in the photonic crystal,[23,24,29,38] as demonstrated in previous studies. These mechanisms can cause an increase in the path length of light, thereby increasing the probability for the photons to be absorbed in the inverse opal photonic crystal.

Figure 7a shows the IPCE curves of the three WO_3 inverse opals, as well as the disordered porous and the unpatterned photoanodes measured at a normal incidence of light. The obtained IPCE of the WO_3-260 inverse opal reaches a value of 18% at 420 nm, which is 1.5−2 times higher than those of the disordered porous and unpatterned WO_3 photoanodes. By normalizing all the IPCE curves to their maximum value at a wavelength of 300 nm, as shown in Figure 7b, we can see that, among all the samples, the IPCE of the WO_3-200 is the most enhanced between 350 and 400 nm, while the IPCE of the WO_3-260 is mostly enhanced between 410 and 460 nm. The normalized IPCE curve of the WO_3-360 matches those of the disordered porous and unpatterned photoanodes.

The IPCE enhancement factor defined as the ratio of the IPCE of the WO_3 inverse opals and disordered porous sample to that of the unpatterned sample was used to reveal the IPCE enhancement features. The IPCE enhancement factor curves are shown in Figure 7c, which clearly indicate that the WO_3 inverse opals especially the WO_3-200 and WO_3-260 samples exhibit selective photoelectric conversion efficiency enhancement in specific spectral regions. Very interestingly, by comparing Figure 7c with Figure 5b, the IPCE enhancement factor curves of the three WO_3 inverse opals are found to show nearly the same variation trends as the absorbance enhancement spectra do (Figure 5b), when the unpatterned WO_3 photoanode is used as a normalized sample.

It is clearly seen that the IPCE enhancement factor curves of two WO_3 inverse opals show an enhancement in the spectral region corresponding to their respective slow-light positions. For example, for the WO_3-200 inverse opal, a higher increase of IPCE resides in the region from 350 to 400 nm, compared with the other photoanodes. This spectral range of IPCE enhancement matches well with the absorption enhancement region from 350 to 420 nm for WO_3-200 (Figure 5b). The WO_3-260 inverse opal has more IPCE enhancement in the spectral regime from 410 to 460 nm. This enhancement regime of WO_3-260 is consistent with its stronger slow-light absorption range of 420−460 nm, which is near the electronic absorption edge of WO_3 (Figure 5b). As for the WO_3-360 inverse opal, its slow-light propagation modes are located far from the electronic absorption of WO_3, and consequently the slow-light effect disappears across

the measured spectrum, leading to a weak dependence of the IPCE curve on the irradiation wavelength. The disordered porous sample is also observed to have a slight increase in IPCE compared with the unpatterned one, as a result of backward scattering in the disordered sample[23,29] and the much larger electrolyte-exposed area in the porous structure, which can induce more effective redox reactions at the WO_3−electrolyte interface.[8,35]

To further investigate the effect of photonic crystal structure on the improvement in the photoelectric conversion efficiency, angle-dependent IPCE measurement was carried out. Figure 8a−c shows the IPCE enhancement factor spectra at two different incident angles of $\theta = 0°$ and 60° as a function of the irradiation wavelength for the three WO_3 inverse opals with different pore sizes. The enhancement factor is calculated by dividing the IPCE of WO_3 inverse opals at 0° and 60° incidence with that of the unpatterned WO_3 photoanode at 0° incidence. The inset is the normalized IPCE curve for each inverse opal sample. Note that the IPCE curves are normalized to their maximum value at a wavelength of 300 nm.

For the WO_3-200 sample (Figure 8a), the normalized IPCE at $\theta = 60°$ shows a further increase in the spectral range 320−390 nm compared with that at $\theta = 0°$. According to the calculation by Bragg's law eq 1, a blue-shift of the stop-band center from 352 to 291 nm is expected for the WO_3-200 inverse opal sample upon increasing the incident angle from 0° to 60°. Thus, this increase of the IPCE is confirmed to be located at the long-wavelength side of the calculated stop-band center at $\theta = 60°$. Moreover, the peak of the IPCE enhancement factor spectrum for WO_3-200 also has a corresponding blue-shift from 0° to 60° incidence, which moves from 400 to 390 nm.

As shown in Figure 8b, a similar effect can be observed for the WO_3-260 photoanode. Increasing the incident angle of light from 0° to 60° leads to a blue-shift in the stop-band center from 427 to 353 nm for WO_3-260 calculated according to eq 1. In this case, the increase of the incident angles makes the slow light at the red-edge of the stop-band, which originally overlapped with the absorption edge of WO_3 under normal incidence of light, move into the electronic absorption range of WO_3. As a result, the peak of the IPCE enhancement factor spectrum for the WO_3-260 changes from 460 to 420 nm as the incident angle increases from 0° to 60°.

However, for the WO_3-360 sample (Figure 8c), the normalized IPCE curves at $\theta = 0°$ and 60° are nearly identical. The magnitude and spectral dependence of the IPCE enhancement factor spectra are similar at $\theta =$ 0° and 60°. This is because the slow-light regime at the red-edge of its stop-band at two incident angles (calculated stop-band center: 578 nm at $\theta = 0°$ and 477 nm at $\theta = 60°$) is far away from the electronic absorption range of WO_3. It is thus demonstrated that the stop-band shift under off-normal incidence could result in the spectral location change of the IPCE enhancement. Our experimental results are consistent with results of a study on dye-sensitized TiO_2 inverse opals by Yip *et al.*[25] They showed through numerical simulations that the electric-field strength enhancement near the red-edge of the stop-band shifted with the incident angle, which was in accordance with the variation of the stop-band.

It has been shown that the top surface layer could play an important role in controlling the interaction of light with photonic crystals.[39−41] For example, García-Santamaría *et al.*[39] have reported that the surface resonance modes generated at the interface of the photonic crystal layer and a dielectric overlayer could be tuned by altering the geometry of the top layer. They found that as the dielectric overlayer was etched away, the surface resonance could be controlled or even eliminated. Lee *et al.*[24] have fabricated a dye-sensitized solar cell (DSSC) that coupled a nanocrystalline TiO_2 underlayer with a TiO_2 inverse opal overlayer. Due to the lack of a close physical contact between the double layers, however, this bilayer configuration resulted in a slight increase of light-harvesting efficiency that was assigned to a rough interface at the bilayer interface. The synthesis route was further improved by Guldin *et al.*, and a smooth interface and intimate physical contact in the bilayer TiO_2 DSSC were obtained.[33] This improved bilayer configuration showed a significant increase of light harvesting in specific parts of the spectrum by photonic-crystal top-layer-induced resonances.

However, the influence of resonant modes induced by different top-layer geometry of photonic crystals on the light-harvesting efficiency is still poorly understood in the field of photoelectrochemistry. For a further study, the top layer of the WO_3 inverse opal as well as the disordered porous structure could be etched away. As the top layer is progressively removed, resonant modes confined within the different patterned top surface could be excited. In this way, the role of the surface resonance as well as of the directional stop-bands in light-harvesting efficiency can be studied and compared. Since this study is beyond the scope of the present work, it will be interesting to exploit these open questions in the future.

CONCLUSIONS

In conclusion, we have demonstrated that photonic crystals can be used to improve the performance of photoelectrochemical devices under visible light irradiation. Inverse opal WO_3 photoanodes with different stop-bands have been prepared. Considerable enhancement of photocurrent intensity has been achieved on the WO_3-260 inverse opal photoanode by adjusting the wavelengths of its slow light close to

the electronic absorption edge of WO_3. The light-harvesting and photon-to-electron conversion efficiency at specific wavelengths is remarkably enhanced by utilization of the slow-light effect in the inverse opals. The spectral range at which photon-to-electron conversion efficiency is enhanced moves to shorter wavelengths as the incident angle increases, which results from a blue-shift in the stop-band center. These results suggest that implementation of the semiconductor photovoltaic device in the form of photonic crystals to manipulate the behavior of the photons and the electrons is a feasible and effective method for enhancing the photon-to-electron conversion efficiency. It will provide useful information for developing other visible-light-sensitive photoanodes with photonic crystal structure.

METHODS

Synthesis of Colloidal Crystal Templates. The colloidal crystal templates were fabricated using a solvent-evaporation-induced convective self-assembly method.[32] A commercially available aqueous PS-sphere solution (Duke Scientific Corp., USA) was mixed with distilled water and polyvinylpyrrolidone (M_w = 55 000; Aldrich, USA);[42] the mixing weight ratios of PS spheres to water and polyvinylpyrrolidone to water were 2×10^{-3} and 1.5×10^{-5}, respectively. The FTO substrate (sheet resistance 30 Ω/cm^2; Asahi Glass Co. Ltd., Japan) was soaked in the mixed H_2SO_4/H_2O_2 aqueous solution with the volume ratio of 3:1 for 1 h and washed with distilled water to make its surface hydrophilic. Subsequently, the hydrophilic FTO substrate was submerged into the prepared PS colloidal suspension. The entire setup was kept at 50 °C in an oven until the water was evaporated. Then 10−15 layers of PS spheres were self-assembled into a close-packing structure on the FTO substrate under capillary forces. To elucidate the photonic crystal effect, a disordered template was also prepared to mold a random WO_3 porous structure as a reference. A clean FTO substrate was placed into a mixed suspension of the PS spheres with diameters of 200, 260, and 360 nm and kept at 50 °C. The weight ratio of PS spheres to water was also 2×10^{-3}. After the water was evaporated, the template with randomly packed spheres was produced.

Synthesis of WO_3 Inverse Opals. WO_3 inverse opals were prepared using $(NH_4)_6H_2W_{12}O_{40}$ solution (Nippon Inorganic Color & Chemical Co. Ltd., Japan)[12] as the precursor. In order to fabricate WO_3 inverse opals with high quality, the forced impregnation approach was used in the infiltration process.[30] The prepared colloidal crystal templates were soaked in a methanol bath for 1 h, and then the templates were taken out of the methanol bath and immersed in a $(NH_4)_6H_2W_{12}O_{40}$ solution bath. During the vacuum impregnation of about 5 h, the precursor permeated into the interstices in the templates easily without destroying the periodicity. After sufficient vacuum impregnation, the coated templates were removed from the precursor bath and were dried in air overnight. Then, the samples were heated to 475 °C at a rate of 1 °C/min and kept at this temperature for 2 h. The disordered porous WO_3 sample was fabricated by the same procedure but using the as-prepared disordered template, and its thickness was controlled around 2.5 μm. The unpatterned WO_3 photoanode of approximately 2.5 μm thick was prepared by the spin-coating method using the same precursor and was sintered under the same experimental conditions as the other photoanodes.

Structural and Optical Characterization. The phase composition of the prepared samples was identified by XRD using Cu Kα radiation (RINT 2000; Rigaku Corp., Japan) in the 2θ range of 15−75°. UV−visible diffuse reflectance spectra were recorded at room temperature on a UV−visible spectrophotometer (UV-2500PC; Shimadzu Corp., Japan) equipped with an integrating sphere. Barium sulfate was used as the normalized source. The reflectance data were transformed into absorbance using the Kubelka−Munk function. The sample morphology was characterized using a scanning electron microscope (JSM-6700F; JEOL, Japan).

Photoelectrochemical Measurement. Photocurrent measurements were performed with an electrochemical station (ALS/CH model 650A, Japan) using a three-electrode mode with 0.1 M Na_2SO_4 solution as the electrolyte. The WO_3 photoanodes were used as working electrodes; a Pt wire served as a counter-electrode. A saturated calomel electrode was used as the reference electrode. The illumination source was a 500 W Xe lamp (Optical ModuleX; Ushio Inc., Japan). The intensity of light at 300−800 nm was measured to be 250 mW/cm^2 using a spectroradiometer (USR-40; Ushio Inc., Japan). Visible light irradiation was performed using a Xe lamp equipped with a UV cutoff filter (L42; Hoya Corp., Japan). In the photocurrent−potential measurement, the WO_3 photoelectrodes were illuminated at normal incidence of light through a quartz window. The voltage-scan speed was 0.01 V/s, and light was chopped manually at regular intervals. For angle-dependent photoelectrochemical measurement, the WO_3 inverse opal photoanodes were irradiated at the specified off-normal angle (60°). The incident photon-to-electron conversion efficiency was obtained with the formula as follows:[43]

$$\mathrm{IPCE} = \frac{hcI}{\lambda P}$$

where P and λ are the intensity (μW cm^{-2}) and the wavelength (nm) of the incident monochromatic light, respectively. I is the photocurrent density (μA cm^{-2}). h and c represent Planck's constant and the speed of light in a vacuum, respectively. The intensity of the incident monochromatic light was measured using the spectroradiometer. Monochromatic irradiation was carried out using the Xe lamp in combination with a monochromator (M10; Jasco Corp., Japan).

Acknowledgment. X.Q.C. thanks Prof. Zhenlin Wang at Nanjing University for fruitful and helpful discussions. This work was partially supported by World Premier International Research Center Initiative (WPI Initiative) on Materials Nanoarchitectonics, the MEXT Program for Development of Environmental Technology using Nanotechnology, the global COE Program of Tokyo Institute of Technology, the Japan Society for the Promotion of Science KAKENHI (21760030), and the National Basic Research Program of China (No. 2007CB613305). The authors thank the anonymous reviewers for their helpful comments on an earlier draft of this paper.

REFERENCES AND NOTES

1. Fujishima, A.; Honda, K. Electrochemical Photolysis of Water at a Semiconductor Electrode. *Nature* **1972**, *238*, 37–38.
2. Grätzel, M. Photoelectrochemical Cells. *Nature* **2001**, *414*, 338–344.
3. Kudo, A.; Miseki, Y. Heterogeneous Photocatalyst Materials for Water Splitting. *Chem. Soc. Rev.* **2009**, *38*, 253–278.
4. Aprile, C.; Corma, A.; Garcia, H. Enhancement of the Photocatalytic Activity of TiO_2 through Spatial Structuring and Particle Size Control: From Subnanometric to Submillimetric Length Scale. *Phys. Chem. Chem. Phys.* **2008**, *10*, 769–783.
5. Santato, C.; Ulmann, M.; Augustynski, J. Photoelectrochemical Properties of Nanostructured Tungsten Trioxide Films. *J. Phys. Chem. B* **2001**, *105*, 936–940.
6. Santato, C.; Ulmann, M.; Augustynski, J. Enhanced Visible Light Conversion Efficiency Using Nanocrystalline WO_3 Films. *Adv. Mater.* **2001**, *13*, 511–514.

7. Santato, C.; Odziemkowski, M.; Ulmann, M.; Augustynski, J. Crystallographically Oriented Mesoporous WO_3 Films: Synthesis, Characterization, and Applications. *J. Am. Chem. Soc.* **2001**, *123*, 10639–10649.
8. Berger, S.; Tsuchiya, H.; Ghicov, A.; Schmuki, P. High Photocurrent Conversion Efficiency in Self-Organized Porous WO_3. *Appl. Phys. Lett.* **2006**, *88*, 203119–203122.
9. Wang, H.; Lindgren, T.; He, J. J.; Hagfeldt, A.; Lindquist, S. E. Photolelectrochemistry of Nanostructured WO_3 Thin Film Electrodes for Water Oxidation: Mechanism of Electron Transport. *J. Phys. Chem. B* **2000**, *104*, 5686–5696.
10. Yang, B.; Zhang, Y.; Drabarek, E.; Barnes, P. R. F.; Luca, V. Enhanced Photoelectrochemical Activity of Sol-Gel Tungsten Trioxide Films through Textural Control. *Chem. Mater.* **2007**, *19*, 5664–5672.
11. Baeck, S. H.; Jaramillo, T.; Stucky, G. D.; McFarland, E. W. Controlled Electrodeposition of Nanoparticulate Tungsten Oxide. *Nano Lett.* **2002**, *2*, 831–834.
12. Sadakane, M.; Sasaki, K.; Kunioku, H.; Ohtani, B.; Ueda, W.; Abe, R. Preparation of Nano-Structured Crystalline Tungsten (VI) Oxide and Enhanced Photocatalytic Activity for Decomposition of Organic Compounds under Visible Light Irradiation. *Chem. Commun.* **2008**, 6552–6554.
13. Arpin, K. A.; Mihi, A.; Johnson, H. T.; Baca, A. J.; Rogers, J. A.; Lewis, J. A.; Braun, P. V. Multidimensional Architectures for Functional Optical Devices. *Adv. Mater.* **2010**, *22*, 1084–1101.
14. Joannopoulos, J. D.; Johnson, S. G.; Winn, J. N.; Meade, R. D. *Photonic Crystals: Molding the Flow of Light*; Princeton University Press: Princeton, 2008; pp 2−3.
15. Sakoda, K. Enhanced Light Amplification due to Group-Velocity Anomaly Peculia to Two- and Three-Dimensional Photonic Crystals. *Opt. Express* **1999**, *4*, 167–176.
16. Baba, T. Slow Light in Photonic Crystals. *Nat. Photonics* **2008**, *2*, 465–473.
17. Lin, S. Y.; Fleming, J. G.; Li, Z. Y.; El-Kady, I.; Biswas, R.; Ho, K. M. Origin of Absorption Enhancement in a Tungsten, Three-Dimensional Photonic Crystal. *J. Opt. Soc. Am. B* **2003**, *20*, 1538–1541.
18. Nagpal, P.; Han, S. E.; Stein, A.; Norris, D. J. Efficient Low-Temperature Thermophotovoltaic Emitters from Metallic Photonic Crystals. *Nano Lett.* **2008**, *8*, 3238–3243.
19. Nishimura, N.; Abrams, N.; Lewis, B. A.; Halaoui, L. I.; Mallouk, T. E.; Benkstein, K. D.; Van de Lagemaat, J.; Frank, A. J. Standing Wave Enhancement of Red Absorbance and Photocurrent in Dye-Sensitized Titanium Dioxide Photoelectrodes Coupled to Photonic Crystals. *J. Am. Chem. Soc.* **2003**, *125*, 6306–6310.
20. Chen, J. I. L.; Von Freymann, F.; Choi, S. Y.; Kitaev, V.; Ozin, A. G. Amplified Photochemistry with Slow Photons. *Adv. Mater.* **2006**, *18*, 1915–1919.
21. Chen, J. I. L.; Von Freymann, F.; Kitaev, V.; Ozin, G. A. Effect of Disorder on the Optically Amplified Photocatalytic Efficiency of Titania Inverse Opals. *J. Am. Chem. Soc.* **2007**, *129*, 1196–1202.
22. Chen, J. I. L.; Loso, E.; Ebrahim, N.; Ozin, G. A. Synergy of Slow Photon and Chemically Amplified Photochemistry in Platinum Nanocluster-loaded Inverse Titania Opals. *J. Am. Chem. Soc.* **2008**, *130*, 5420–5421.
23. Halaoui, L. I.; Abrams, N. M.; Mallouk, T. E. Increasing the Conversion Efficiency of Dye-Sensitized TiO_2 Photoelectrochemical Cells by Coupling to Photonic Crystals. *J. Phys. Chem. B* **2005**, *109*, 6334–6342.
24. Lee, S.-H. A.; Abrams, N. M.; Hoertz, P. G.; Barber, G. D.; Halaoui, L. I.; Mallouk, T. E. Coupling of Titania Inverse Opals to Nanocrystalline Titania Layers in Dye-Sensitized Solar Cells. *J. Phys. Chem. B* **2008**, *112*, 14415–14421.
25. Yip, C.-H.; Chiang, Y.-M.; Wong, C.-C. Dielectric Band Edge Enhancement of Energy Conversion Efficiency in Photonic Crystal Dye-Sensitized Solar Cell. *J. Phys. Chem. C* **2008**, *112*, 8735–8740.
26. Liu, J.; Li, M.; Wang, J.; Song, Y.; Jiang, L.; Murakami, T.; Fujishima, A. Hierarchically Macro-/Mesoporous Ti-Si Oxides Photonic Crystal with Highly Efficient Photocatalytic Capability. *Environ. Sci. Technol.* **2009**, *43*, 9425–9431.
27. Liao, G.; Chen, S.; Quan, X.; Chen, H.; Zhang, Y. Photonic Crystal Coupled TiO_2/Polymer Hybrid for Efficient Photocatalysis under Visible Light Irradiation. *Environ. Sci. Technol.* **2010**, *44*, 3481–3485.
28. Chen, H.; Chen, S.; Quan, X.; Zhang, Y. Structuring a TiO_2-Based Photonic Crystal Photocatalyst with Schottky Junction for Efficient Photocatalysis. *Environ. Sci. Technol.* **2010**, *44*, 451–455.
29. El Harakeh, M.; Halaoui, L. Enhanced Conversion of Light at TiO_2 Photonic Crystals to the Blue of a Stop Band and at TiO_2 Random Films Sensitized with Q-CdS: Order and Disorder. *J. Phys. Chem. C* **2010**, *114*, 2806–2813.
30. Chen, X.; Li, Z.; Ye, J.; Zou, Z. Forced Impregnation Approach to Fabrication of Large-Area, Three-Dimensionally Ordered Macroporous Metal Oxides. *Chem. Mater.* **2010**, *22*, 3583–3585.
31. Ren, M. M.; Ravikrishna, R.; Valsaraj, K. T. Photocatalytic Degradation of Gaseous Organic Species on Photonic Band-Gap Titania. *Environ. Sci. Technol.* **2006**, *40*, 7029–7033.
32. Jiang, P.; Bertone, J. F.; Hwang, K. S.; Colvin, V. L. Single-Crystal Colloidal Multilayers of Controlled Thickness. *Chem. Mater.* **1999**, *11*, 2132–2140.
33. Guldin, S.; Huttner, S.; Kolle, M.; Welland, M. E.; Muller-Buschbaum, P.; Friend, R. H.; Steiner, U.; Tetreault, N. Dye-Sensitized Solar Cell Based on a Three-Dimensional Photonic Crystal. *Nano Lett.* **2010**, *10*, 2303–2309.
34. Li, X.; Jiang, Y.; Shi, Z. W.; Xu, Z. Two Growth Modes of Metal Oxide in the Colloidal Crystal Template Leading to the Formation of Two Different Macroporous Materials. *Chem. Mater.* **2007**, *19*, 5424–5430.
35. Kwak, E. S.; Lee, W.; Park, N. G.; Kim, J.; Lee, H. Compact Inverse-Opal Electrode Using Non-Aggregated TiO_2 Nanoparticles for Dye-Sensitized Solar Cells. *Adv. Funct. Mater.* **2009**, *19*, 1093–1099.
36. Mihi, A.; Calvo, M. E.; Anta, J. A.; Míguez, H. Spectral Response of Opal-Based Dye-Sensitized Solar Cells. *J. Phys. Chem. C* **2008**, *112*, 13–17.
37. Mittleman, D.; Bertone, J.; Jiang, P.; Hwang, K.; Colvin, V. Optical Properties of Planar Colloidal Crystals: Dynamical Diffraction and The Scalar Wave Approximation. *J. Chem. Phys.* **1999**, *111*, 345–354.
38. Ramiro-Manzano, F.; Atienzar, P.; Rodriguez, I.; Meseguer, F.; Garciab, H.; Corma, A. Apollony Photonic Sponge Based Photoelectrochemical Solar Cells. *Chem. Commun.* **2007**, 242–244.
39. García-Santamaría, F.; Nelson, E. C.; Braun, P. V. Optical Surface Resonance May Render Photonic Crystals Ineffective. *Phys. Rev. B* **2007**, *76*, 075132.
40. Mihi, A.; Míguez, H.; Rodríguez, I.; Rubio, S.; Meseguer, F. Surface Resonant Modes in Colloidal Photonic Crystals. *Phys. Rev. B* **2005**, *71*, 125131.
41. Mihi, A.; Míguez, H. Origin of Light-Harvesting Enhancement in Colloidal-Photonic-Crystal-Based Dye-Sensitized Solar Cell. *J. Phys. Chem. B* **2005**, *109*, 15968–15976.
42. Choi, H. K.; Kim, M. H.; Im, S. H.; Park, O. O. Fabrication of Ordered Nanostructured Arrays Using Poly(dimethylsiloxane) Replica Molds Based on Three-Dimensional Colloidal Crystals. *Adv. Funct. Mater.* **2009**, *19*, 1594–1599.
43. Sayama, K.; Nomura, A.; Arai, T.; Sugita, T.; Abe, R.; Yanagida, M.; Oi, T.; Iwasaki, Y.; Abe, Y.; Sugihara, H. Photoelectrochemical Decomposition of Water into H_2 and O_2 on Porous $BiVO_4$ Thin-Film Electrodes under Visible Light and Significant Effect of Ag Ion Treatment. *J. Phys. Chem. B* **2006**, *110*, 11352–11360.